Supplementary Information

Ultrathin amorphous defective co-doped hematite passivation layer derived via in-situ electrochemical method for durable photoelectrochemical water oxidation

Milad Fathabadi,[1] Mohammad Qorbani,[2,3,✉] Amr Sabbah,[4,5] Shaham Quadir,[2,4,6,7] Chih-Yang Huang,[2,3,6,8] Kuei-Hsien Chen,[2,4] Li-Chyong Chen,[2,3,9,✉] and Naimeh Naseri[1,✉]

[1]Department of Physics, Sharif University of Technology, Tehran 11155-9161, Iran.

[2]Center for Condensed Matter Sciences, National Taiwan University, Taipei 10617, Taiwan.

[3]Center of Atomic Initiative for New Materials, National Taiwan University, Taipei 10617, Taiwan.

[4]Institute of Atomic and Molecular Sciences, Academia Sinica, Taipei 10617, Taiwan.

[5]Tabbin Institute for Metallurgical Studies, Tabbin, Helwan 109, Cairo 11421, Egypt.

[6]Molecular Science and Technology Program, Taiwan International Graduate Program, Academia Sinica, Taipei 11529, Taiwan.

[7]Department of Physics, National Central University, Taoyuan City 32001, Taiwan.

[8]International Graduate Program of Molecular Science and Technology, National Taiwan University, Taipei, 10617, Taiwan.

[9]Department of Physics, National Taiwan University, Taipei 10617, Taiwan.

[✉]E-mail: mqorbani@ntu.edu.tw (M. Q.), chenlc@ntu.edu.tw (L.-C. C.), and naseri@sharif.edu (N. N.)

Contents

Supplementary Notes

Note S1. Photoanode preparation

A piece of fluorine-doped tin oxide (FTO;15 Ω sq^{-1}) substrate was carefully cleaned by a sonication process in a diluted soap solution, deionized (DI) water, acetone, ethanol, and DI water, successively followed by drying at 100 ºC in an oven. The α-Fe_2O_3 layer was then formed on the FTO through a two-step procedure reported previously, *i.e.*, hydrothermal process followed by an annealing process.[1] (*i*) The hydrothermal method was used to grow the β-FeOOH layer on the FTO. 20 mL aqueous solution, containing 0.15 M iron (III) chloride hexahydrate ($FeCl_3.6H_2O$; Merck) and 1 M sodium nitrate ($NaNO_3$; Merck) was prepared at room temperature. For the doped hematite, different amounts of titanium (IV) n-butoxide ($Ti[O(CH_2)_3CH_3]_4$, ≥ 98 ACROS Organics) were dissolved in 50 µL of hot hydrochloric acid (HCl, 37% ACS Merck, keeping at the temperature of ~48°C), to adjust pH between 1.3 and 1.5 and solve the titanium (IV) n-butoxide, as the precursor. The aqueous solution was then added to that and all solution was transferred to the 100 mL Teflon-lined autoclave which contained the FTO substrate was placed with the conductive side towards the autoclave wall. Then, the autoclave was put in the oven at 95 °C to form the β-FeOOH layer on the substrate. The hydrothermal time of forming the β-FeOOH layer was 4 h for bare hematite and 13 h for Ti-doped hematite. To compare the effect of the active material thickness on the photoelectrochemical performance, Ti-doped hematite was also grown for 24 h. Afterward, the FTO was washed with DI water and dried at 60 ºC. (*ii*) The prepared films were transferred to the furnace and annealed at 550 ºC for 3 h with a ramping rate of 10 °C min^{-1} to form α-Fe_2O_3. The nominal ratios of Ti–to–(Fe+Ti) were $x_c = \frac{Ti}{Ti+Fe}$ = 0%, 0.5%, 1.0%, 1.5%, and 2.0%. These Ti-doped Fe_2O_3 samples were named TFO in the present manuscript.

Note S2. Electrochemical formation of the passivation layer

The passivation layer was formed by a cyclic voltammetry (CV) with a scan rate of 5 mV s^{-1} in a three-electrode system. First, we have determined the suitable potential window; and next, the number of CV cycles was optimized. The applied potential windows were 0 to -0.2 (ΔV = 0.2 V; where ΔV is the potential difference), 0 to - 0.4 (ΔV = 0.4 V), 0 to -0.6 (ΔV = 0.6 V), 0 to -0.8 (ΔV = 0.8 V), 0 to -1.0 (ΔV = 1.0 V), 0 to -1.2 V (ΔV = 1.2 V), and 0 to - 1.4 (ΔV = 1.4 V) vs. Ag/AgCl. Then, the number of CV cycles was optimized at the optimized potential difference of ΔV = 1.2 V. All the passivation processes were performed in a 1 M KOH aqueous solution. The TFO samples passivated by the electrochemical method are called EP-TFO.

Note S3. Characterizations

The X-ray diffraction (XRD) patterns were recorded using a Cu K_α radiation source (Bruker, D2 PHASER with XFlash) to determine the crystal structure. X-ray photoelectron spectroscopy (XPS) measurements were collected using a Theta Probe Thermo Scientific with a micro-focused electron gun, multi-position aluminum anode, and a monochromated X-ray source. XPS spectra were calibrated by the C 1*s* peak at 284.6 eV. The CasaXPS software was used to fit the XPS data with Gaussian–Lorentzian line shapes. Surface morphologies and microstructures were recorded by field-emission scanning electron microscopy (FESEM, JEOL, 6700F) and high-resolution transmission electron microscopy (HRTEM, JEOL–2100) at 6 kV and 200 kV, respectively. The elemental composition was investigated by high-angle annular dark-field (HAADF) image and energy-dispersive X-ray spectroscopy (EDX). HRTEM (JEOL-2100) with selected area electron diffraction (SAED) and EDX to determine the crystal phase, and elemental compositions. Dark-field STEM was performed on JEM-ARM300F2 (aka Grand ARM2) with a probe and image aberration correctors by JEOL Ltd. Japan. The

ultraviolet–visible (UV–Vis.) reflectance spectra were measured by a Jasco V–670 spectrophotometer using an integrated sphere and collected data was converted from reflection to absorbance using the Kubelka–Munk function. Raman scattering measurements were performed using 473 nm and 532 nm continuous-wave lasers coupled with an optical fiber to NTEGRA Spectra; NT–MDT and iHR550 Horiba Jobin Yvon spectrometers, respectively. For time-resolved photoluminescence (TRPL) measurements and intensity-dependent PL experiments, a 405 nm pulse laser with the repetition rate of 40 MHz was used to excite the sample coupled with spectrometer Horiba JOBIN YVON system (iHR550 monochromator), a CCD (HORIBA Scientific's symphony CCD camera), and PMT (PicoQuant PMA192 PMT). TRPL measurement was performed by a time-correlated single-photon counting (TCSPC) system. A cryogenic stage (Linkam BCS196) equipped with the 405 nm laser, under liquid N_2 (Linkam LNP96 cooling system), was used to perform the low-temperature experiments. Moreover, the composition was measured by X-ray fluorescence (XRF) measurement (XRF–1800, Shimadzu Scientific Instruments). Height profiles were recorded by using Bio-AFM (Ara Research Co.) and a Bruker Dimension Icon system. Amplitude modulated Kelvin probe force microscopy (AM-KPFM) was used to locally map the work function of the sample after calibration of the probe work function on a gold film. So, an alternating current voltage of 1.5 V at a frequency of 73 kHz was applied to a Pt/Ir coated probe.[2] Notably, the height profile also was measured in the same mode. Inductively coupled plasma (ICP) measurements were performed by a Varian (ICP-OES 730-ES) system. For the ICP test, 40 ml of the electrolyte solution (the volume of the electrolyte solution was 120 ml) was removed and re-filled by a fresh one after each electrochemical cycle. So, the measured amount of the ions was calculated accordingly.

Note S4. Photoelectrochemical water oxidation

Photoelectrochemical (PEC) performances of electrodes were investigated by a three-electrode workstation (Potentiostat OrigaF010). Pt wire and Ag/AgCl (3 M KCl) were used as the counter and reference electrodes, respectively. All samples were illuminated by a Xe lamp with a solar-like irradiation spectrum and an intensity of 100 mW cm^{-2}. All PEC tests were measured in a 1 M KOH aqueous solution. Electrochemical impedance spectroscopy (EIS) measurements at fixed potential were performed in a frequency range of 100 kHz to 100 mHz at 0.5 V vs. Ag/AgCl in dark and under light irradiation. EIS data was analyzed by EIS Spectrum Analyser software (version 1.0). The following equation was used to calibrate potential, $V_{RHE} = V_{Ag/AgCl} + 0 \cdot 059\ pH + 0 \cdot 198$, where V_{RHE} and $V_{Ag/AgCl}$ are the potentials of reversible hydrogen (RHE) and Ag/AgCl reference electrodes, respectively. Further, the H_2 and O_2 products were measured by a gas chromatography system (GC, HP 6890) equipped with a helium ionization detector (HID) equipped with ShinCarbon ST Packed Column (2.0 m/3.175mm/2.0 mm) for products separation.

Note S5. Photoelectrochemical stability test

The short-term PEC stability of the electrodes was measured for 10 h. The photocurrent density was recorded for 1 hour and then, the electrodes were removed from the cell to remove oxygen bubbles from the surface of the photoanodes. So, ten successive cycles have been performed for the stability of the electrodes. The long-term PEC stability of the electrodes was measured for 96 h. Initially, we recorded the photocurrent density for 12 h for a non-passivated sample. Then, a passivation process was performed and the photocurrent density was recorded for 12 h, afterwards, the electrodes were removed from the cell to remove oxygen bubbles from the surface of the photoanodes. Notably, we carried out a passivation process after each 24 h.

Note S6. Optimization of Ti concentration

TFO photoanodes were synthesized using a well-developed hydrothermal method.[3-5] It is well-known that the thickness of the film reached a maximum after a certain time, which is a function of the initial Ti concentration. For example, Yang et al. have shown that adding Ti precursor decreases the growth rate.[1] Ti ions promote fast nucleation and exhaust the Fe ions concentration, resulting in less film thickness.[6] In a nutshell, Ti dopant can increase the electrical conductivity of the film but prevent the film reaches to the suitable thickness, which is required for efficient light harvesting. Regarding the competition among electrical conductivity, light absorption, and charge carrier diffusion length, an optimum nominal concentration of Ti ($x_c = \frac{Ti}{Ti+Fe}$) could be obtained for the best PEC performance. As shown in Fig. S1–Fig. S2, the thickness of the TFO photoanodes decreases with increasing x_c. Notably, the cross-sectional FESEM images show that the films consist of interconnected nanorods. X-ray diffraction patterns (XRD) display an intense peak at 35.8° and two small peaks at 33.3° and 64.1° assigned to (110), (104), and (300) planes (corresponding to the trigonal space group $R\bar{3}c$, JCPDS 33-0664), respectively (Fig. S3). It also displays that the crystal structure does not change due to the introduction of the Ti into the lattice of the hematite. As expected, we do not observe obvious peak shifts via the doping of Ti (see the inset of Fig. S3 which compare the pristine and optimized samples). For example, it has been presented that the introduction of 23.1% Ti, which is approximately one order of magnitude larger than our work (see the following text), into the lattice of the hematite shows a slight shift of ≤ 0.2° in peak position toward lower angles.[7] Further, a strong (110) peak indicates that the nanorods are oriented in the [110] crystalline direction that is known as preferential well-conducting orientation [8]. Raman scattering spectra show a blue-shift in the lattice vibrational modes (ω) of the TFO by increasing x_c (Fig. S4). This can be explained by the harmonic oscillator model, i.e., $\omega = \sqrt{k/\mu}$,

where k and μ are the restoring force constant and reduced mass, respectively. That means μ decreases by substituting the lighter Ti element into the heavier Fe sites. UV–visible absorption spectra show that the bandgap of the TFO enlarges from ~2.0 eV (for the pristine sample) to ~2.1 eV (for the x_c = 2.0%) (Fig. S5). Moreover, introducing Ti alleviates the mid-gap states, known as the Urbach tail [9], which can result in less bulk recombination of the photogenerated charge carriers. Fig. S6 shows the linear sweep voltammetry (LSV) curves of the prepared electrodes in dark and under light irradiation. It reveals that the photoresponse reaches a maximum value for x_c = 1.0% (optimum electrode), which is two orders of magnitude larger than the pristine hematite at 0.5 $V_{Ag/AgCl}$. The PEC performance of the optimum electrode can be assigned to the smaller overall charge transfer resistance (Fig. S7) and appropriate thickness (~270 ± 20 nm) for light-harvesting and photogenerated charge carrier diffusion length (Fig. S8). Further, energy-dispersive X-ray spectroscopy (EDX) (Fig. S9a–b) and X-ray fluorescence (XRF) measurement represent that the actual Ti concentration inside the hematite lattice is about 3.4% ± 0.5% and 3.2% ± 0.3%, respectively. Moreover, elemental mapping EDX reveals that Fe, O, and Ti elements are uniformly distributed in the grown film (Fig. S9c).

Supplementary Figures

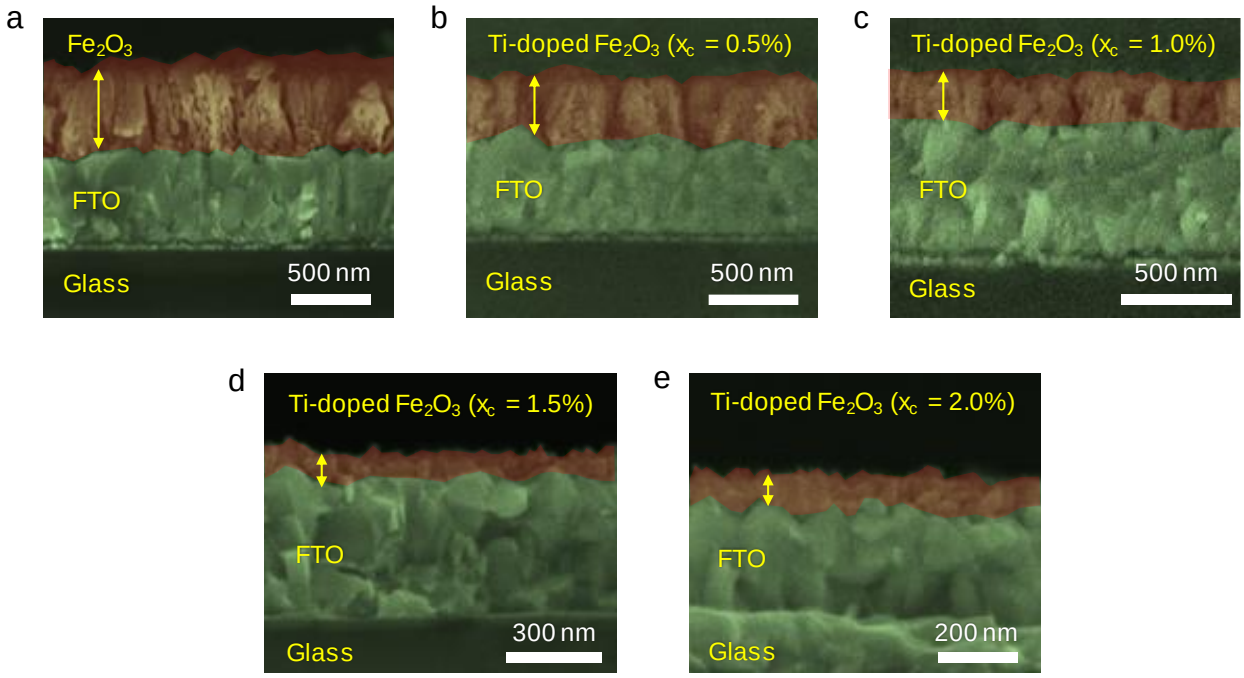

Figure S1. Cross-sectional FESEM images. (a) to (e) FESEM images of the prepared samples for different concentrations of Ti, i.e., x_c = 0% to 2.0%, respectively. Notably, the growth times of the hydrothermal process are 4 h for the pristine Fe_2O_3 (x_c = 0%) and 13 h for the TFO photoanodes.

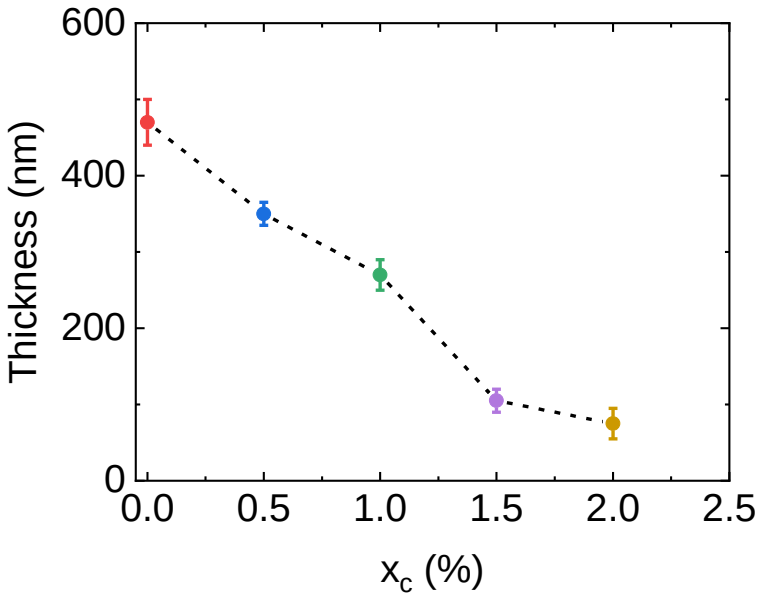

Figure S2. Thickness of the photoanodes. The thickness of the prepared samples as a function of x_c. Notably, the growth times of the hydrothermal process are 4 h for the pristine Fe_2O_3 (x_c = 0%) and 13 h for the TFO photoanodes.

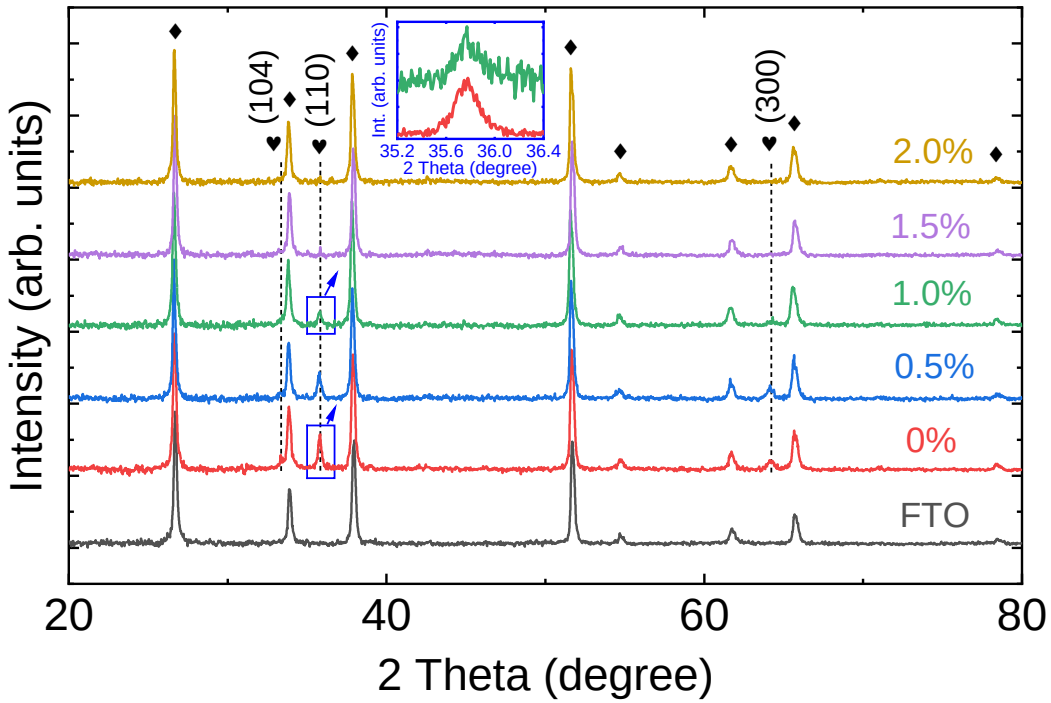

Figure S3. Crystalline structures. X-ray diffraction patterns of the FTO substrate, pristine F_2O_3 (x_c = 0%), and TFO samples. Diamond (♦) and hart (♥) symbols stand for the peaks belonging to the FTO and TFO samples, respectively. The signal of the (110) and (300) peaks decreases (~74%) by increasing x_c to 2.0%, consisting of the reduction (~77%) of the film thickness at high x_c. Inset shows the zoomed XRD peaks of x_c = 0 and 1%.

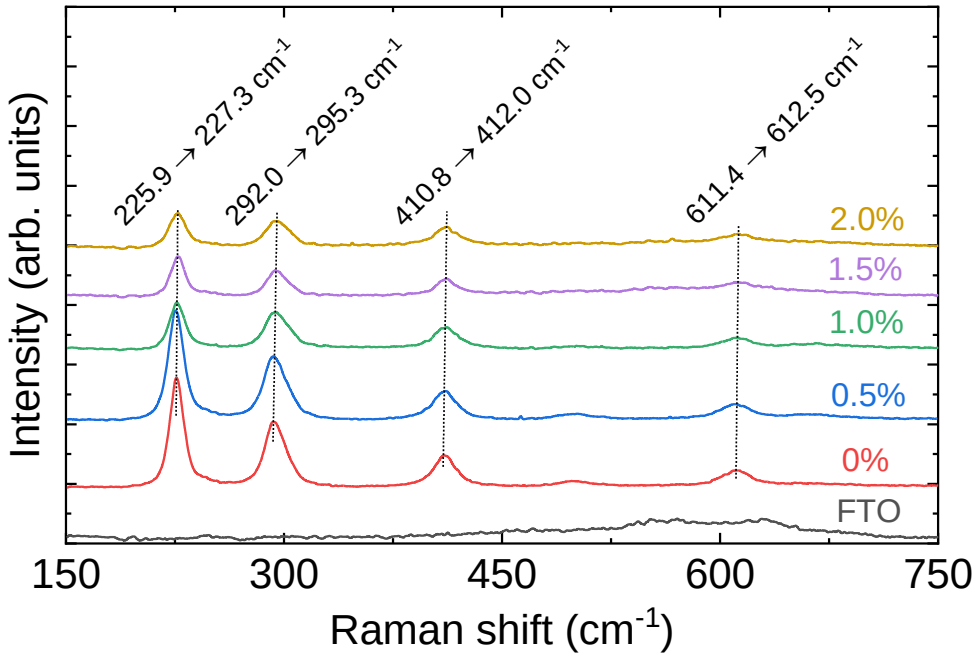

Figure S4. Lattice vibrational modes. Raman scattering spectra of the FTO substrate, pristine Fe_2O_3 (x_c = 0%), and TFO samples using a continuous-wave laser with the wavelength of 473 nm.

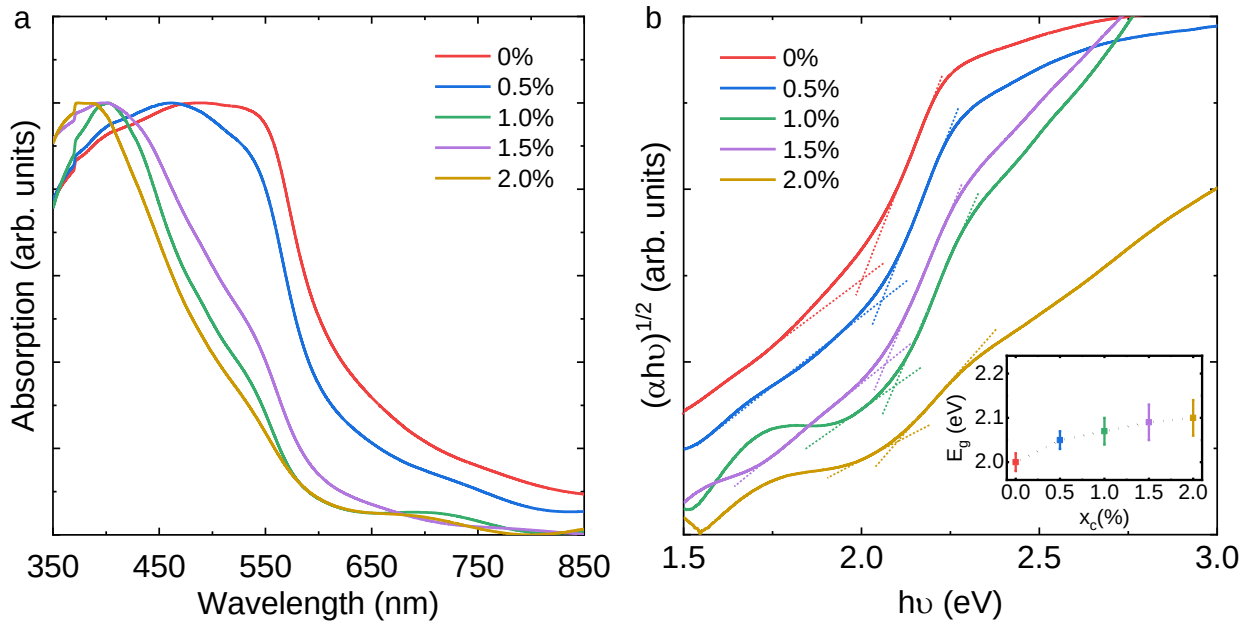

Figure S5. Optical properties. (a) and (b) UV–visible absorption spectra and the Tauc plots, respectively. The inset of (b) shows the indirect band gap versus the nominal concentration of Ti dopant.

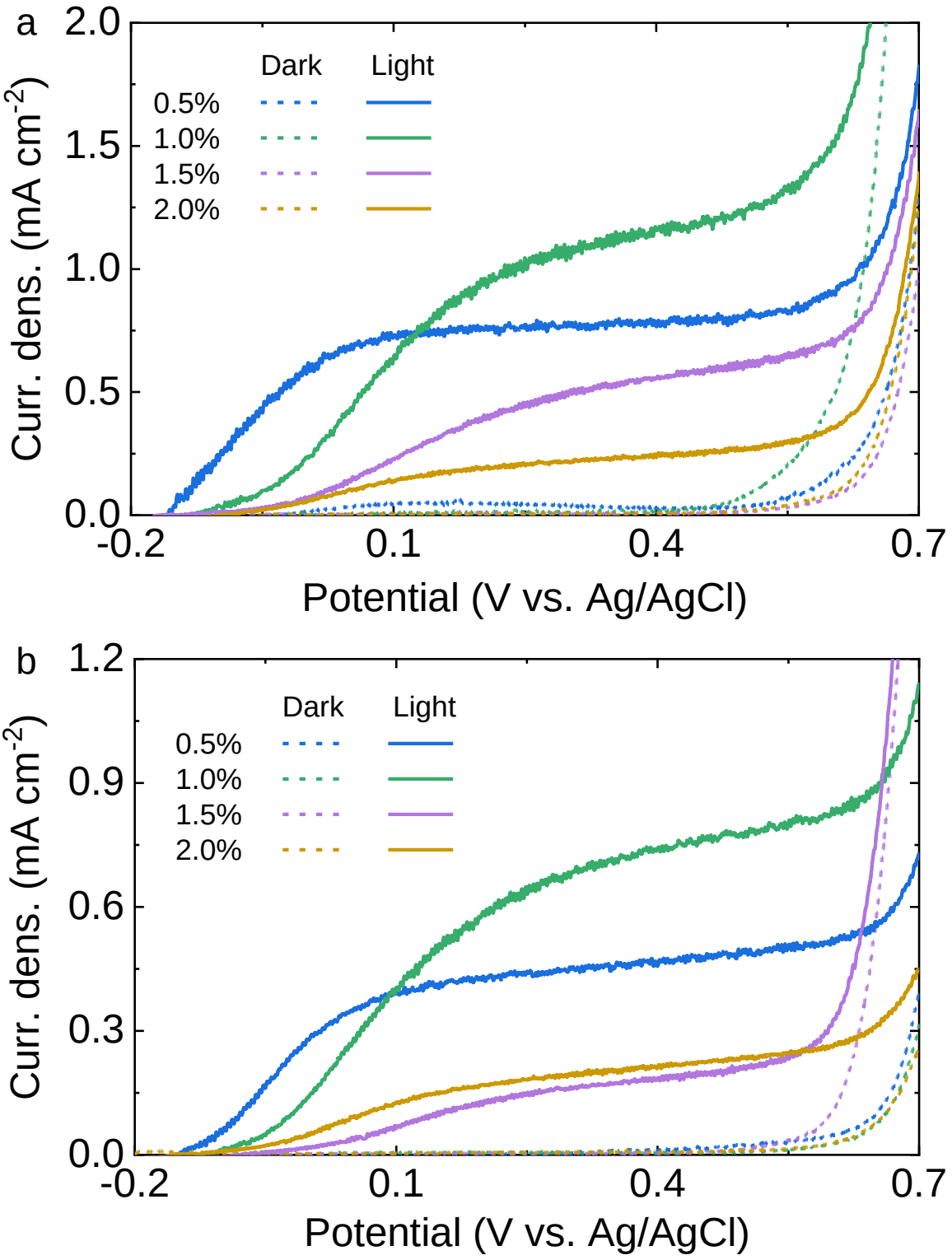

Figure S6. Photoelectrochemical responses of the TFOs. Linear sweep voltammetry (LSV) curves in dark and under light irradiation for the samples with hydrothermal growth time of (a) 13 h and (b) 24 h, respectively.

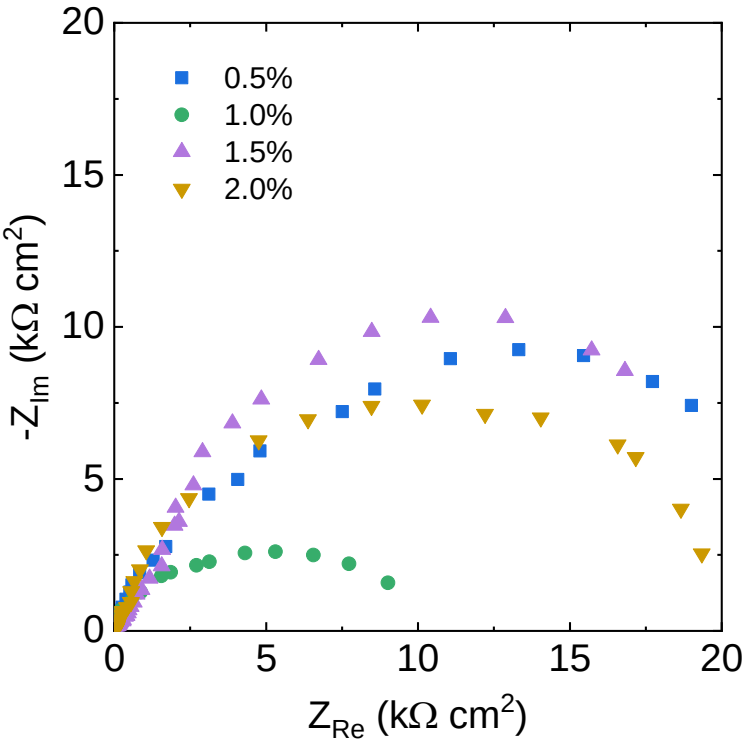

Figure S7. Electrochemical impedance spectroscopy of the TFOs. Nyquist plots at 0.5 $V_{Ag/AgCl}$ in dark. x_c = 1.0% shows the smallest overall charge transfer resistance.

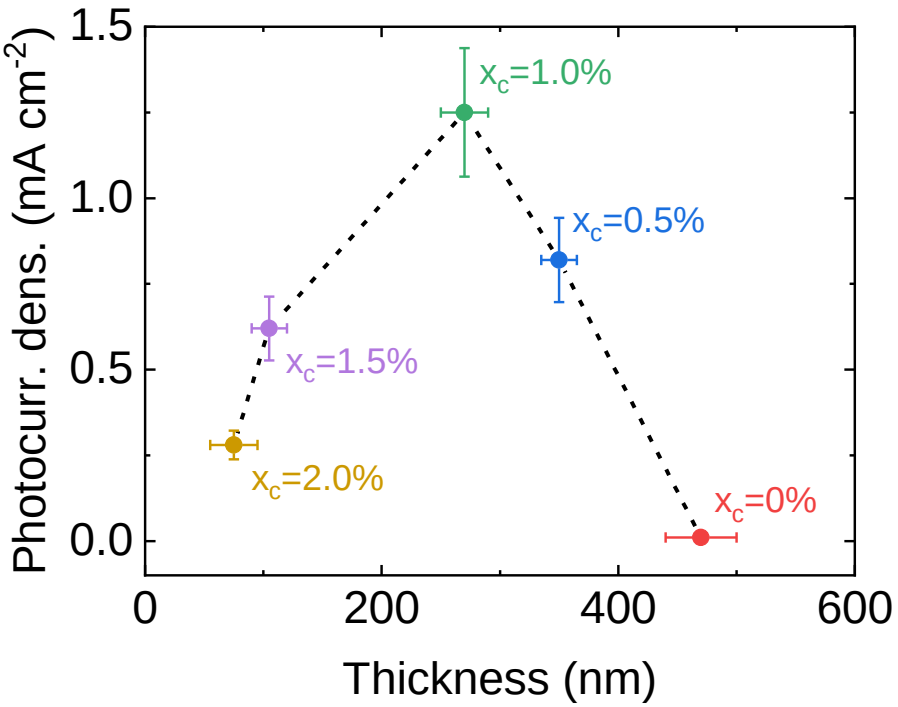

Figure S8. Thickness-dependent electrochemical performance. Photocurrent density versus the thickness of the photoanodes.

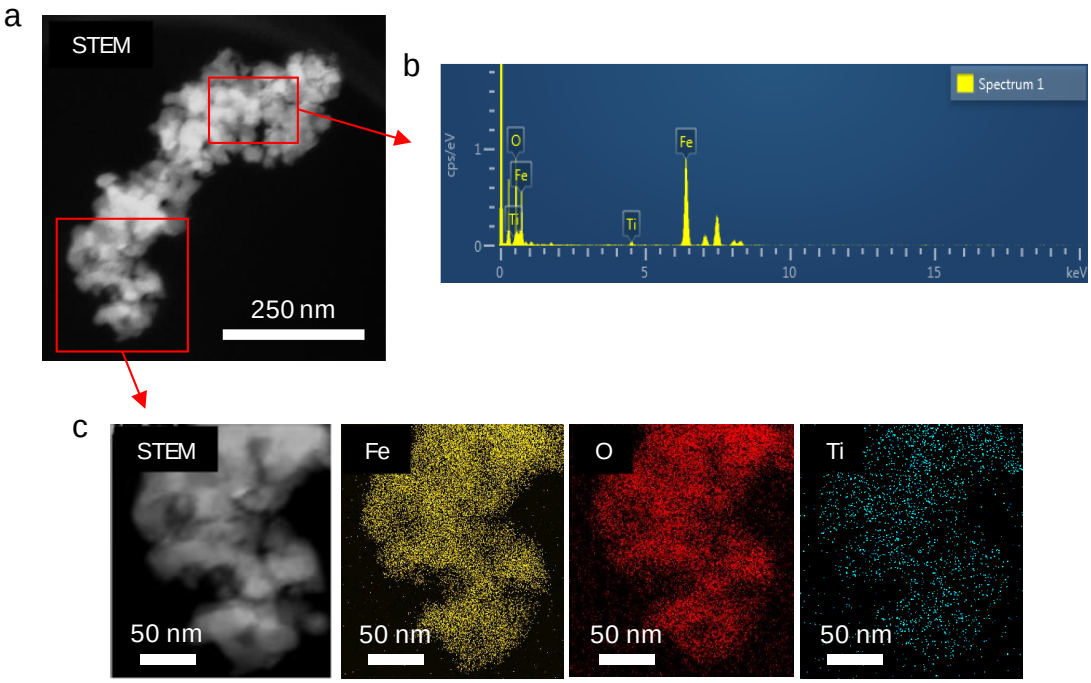

Figure S9. EDX of the Ti-doped (x_c = 1.0%) Fe_2O_3. (a) Scanning transmission electron microscope (STEM) image. (b) EDX spectrum of the assigned region. (c) STEM image and corresponding EDX elemental mapping images of the Fe, O, and Ti elements.

Figure S10. The effect of the passivation voltage. Passivation under applied potential of ΔV = 1.4 and 1.2 $V_{Ag/AgCl}$.

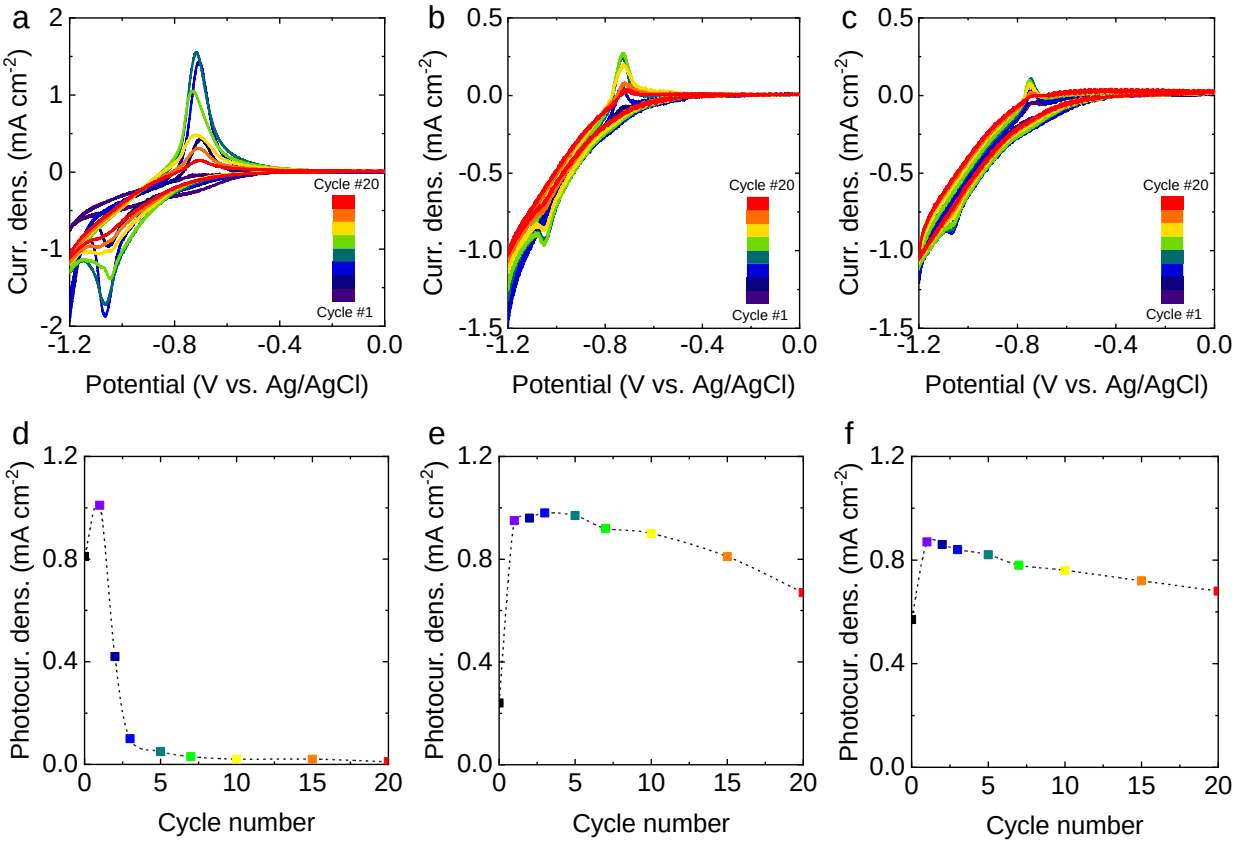

Figure S11. Electrochemical passivation of the TFOs ($x_c \neq$ 1.0%). (a,d), (b,e), and (c,f) CV cycles and photocurrent density of the electrodes with x_c = 0.5%, 1.5%, and 2.0%, respectively.

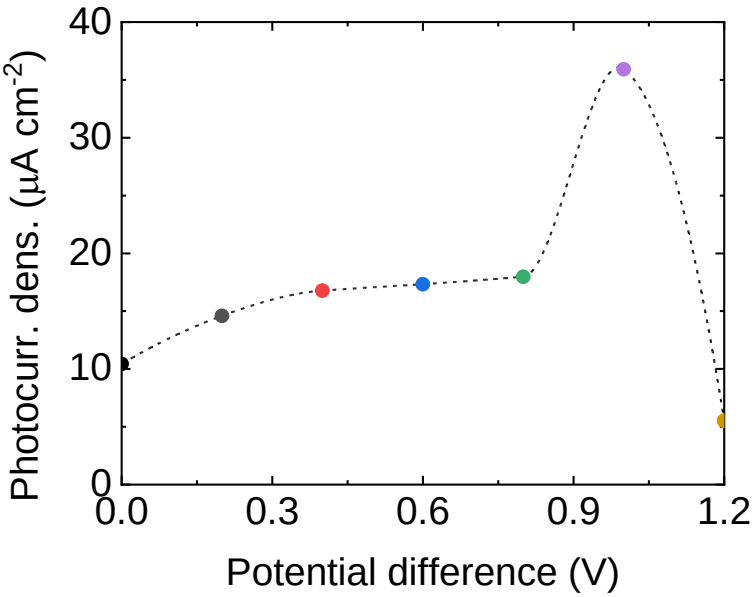

Figure S12. Electrochemical passivation of the pristine Fe_2O_3 photoanode. Photocurrent density under light irradiation versus the potential difference.

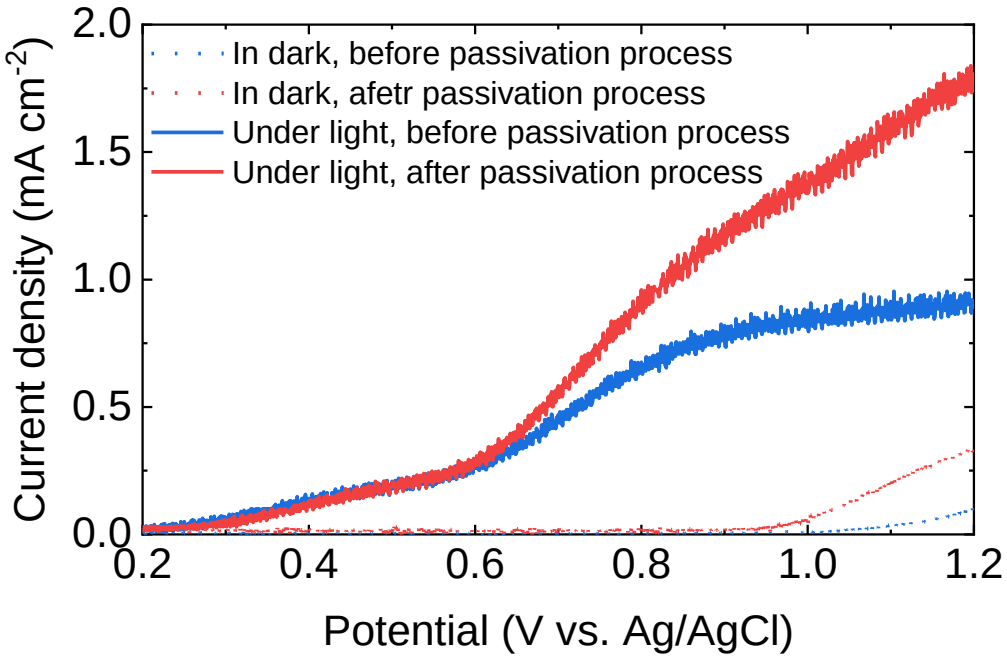

Figure S13. Electrochemical passivation of the TFOs (x_c = 1.0%) in neutral electrolyte. LSV curves in dark and under light irradiation of the EP-TFO photoanodes in 1 M Na_2SO_4 electrolyte before and after passivation process.

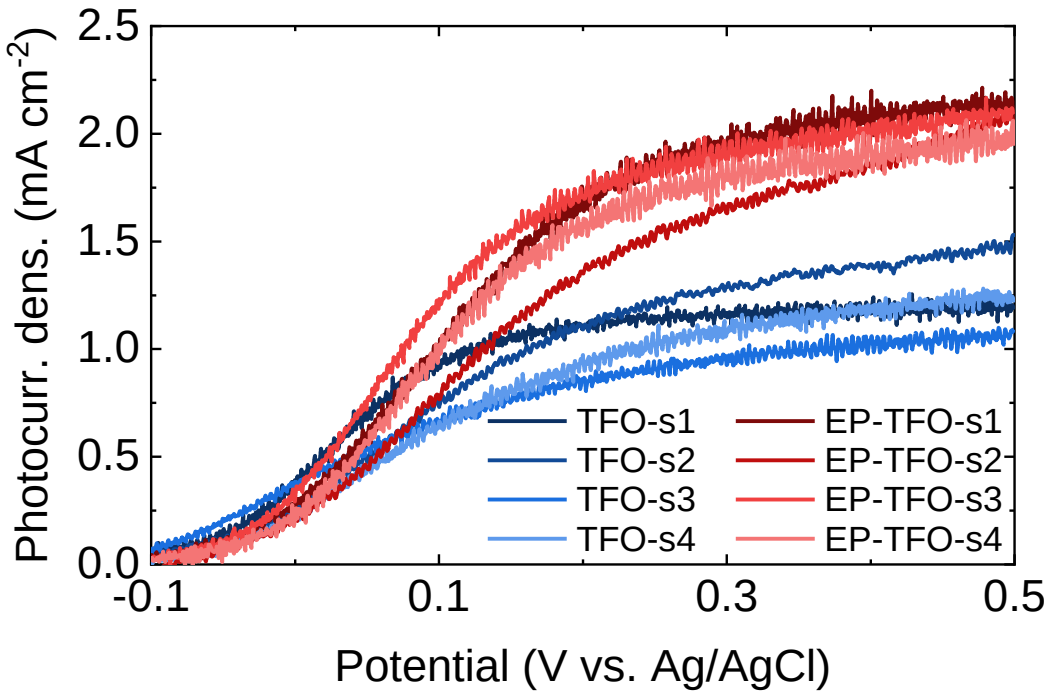

Figure S14. Onset potential under light. LSV curves under light irradiation of the TFO and EP-TFO photoanodes with x_c = 1.0%.

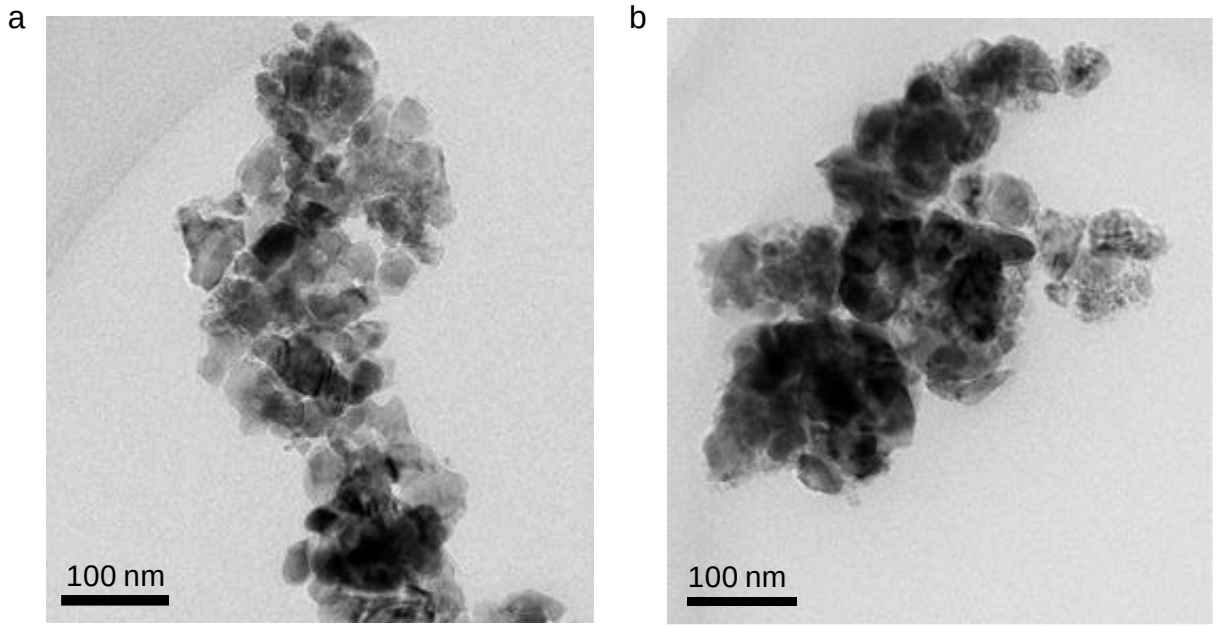

Figure S15. Grain sizes. (a) and (b) TEM images of the TFO and EP-TFO samples. These images show that the grain sizes are in the range of 50 to 100 nm, which did not change after the electrochemical passivation process.

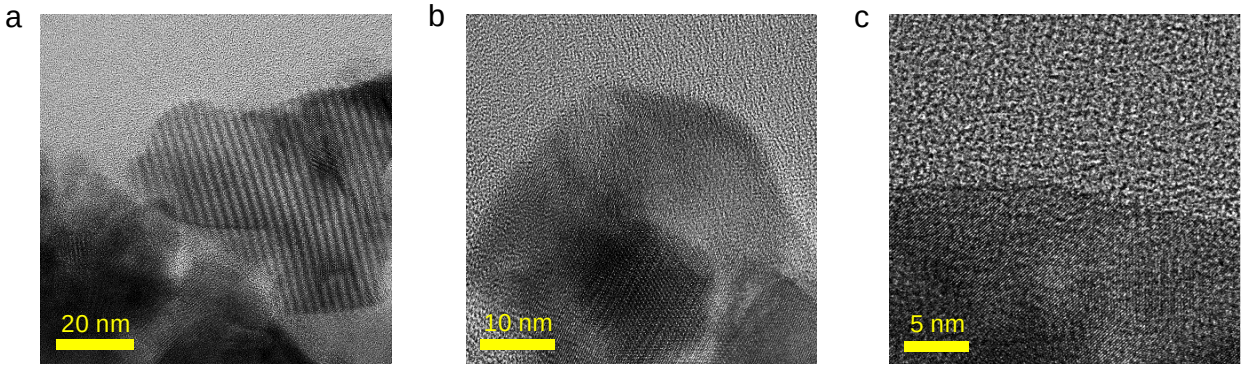

Figure S16. Microstructure of the TFO. TEM and HRTEM images at different magnifications of (a) 300 kX (b) 600 kX, and (c) 1 MX.

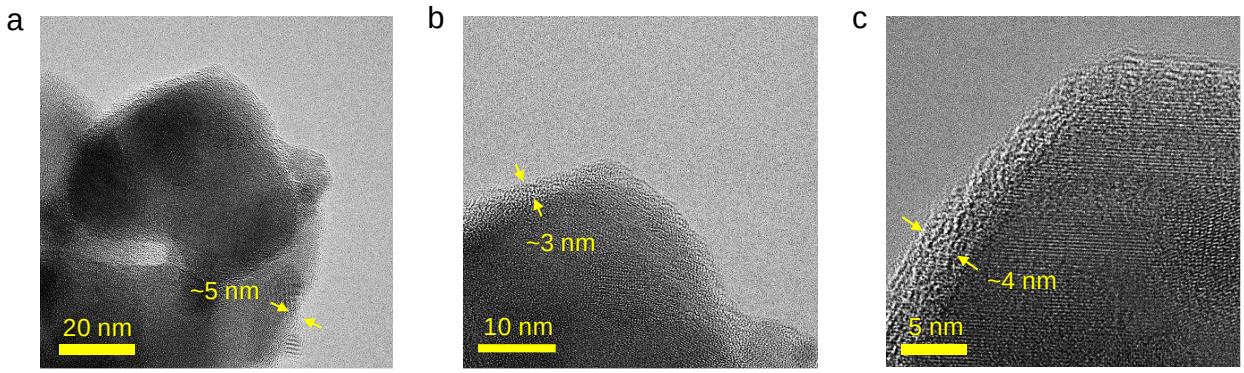

Figure S17. Microstructure of the EP-TFO. TEM and HRTEM images at different magnifications of (a) 300 kX (b) 600 kX, and (c) 1 MX.

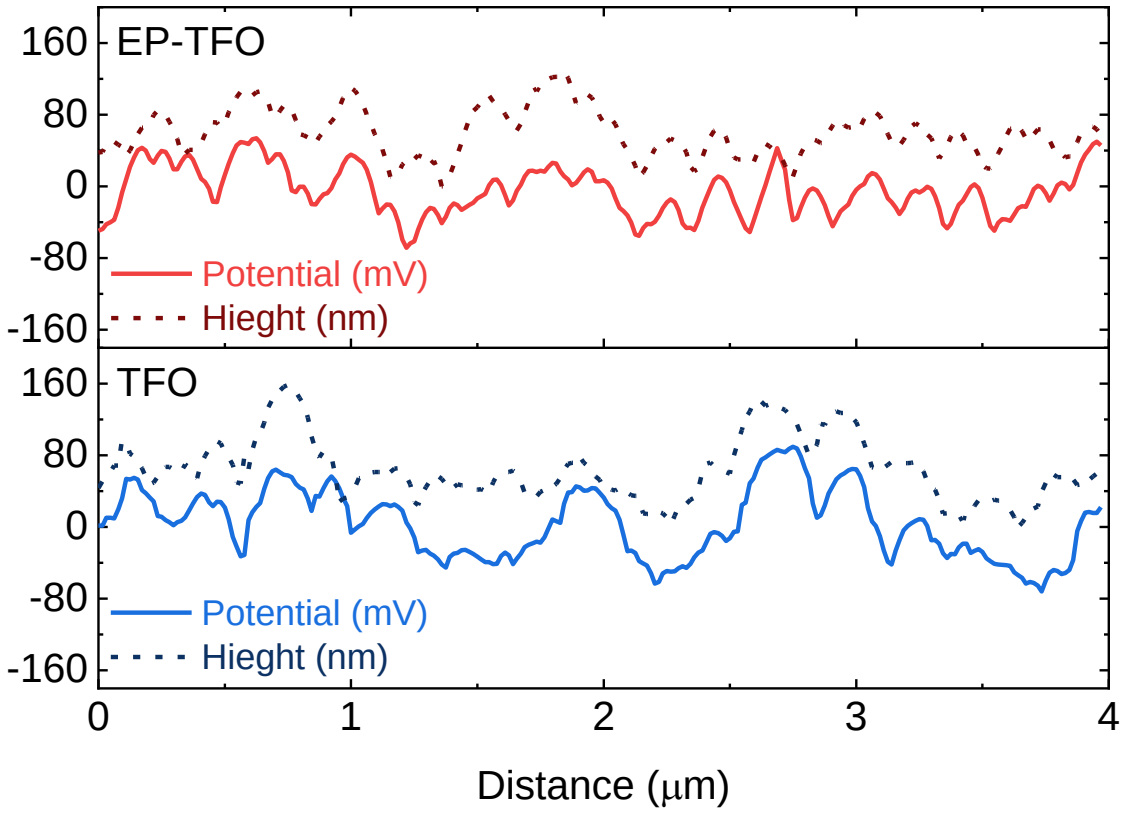

Figure S18. KPFM potential fluctuation. The surface potential and height profiles of the TFO and EP-TFO samples of the dashed lines are shown in Fig. 3c in the main manuscript.

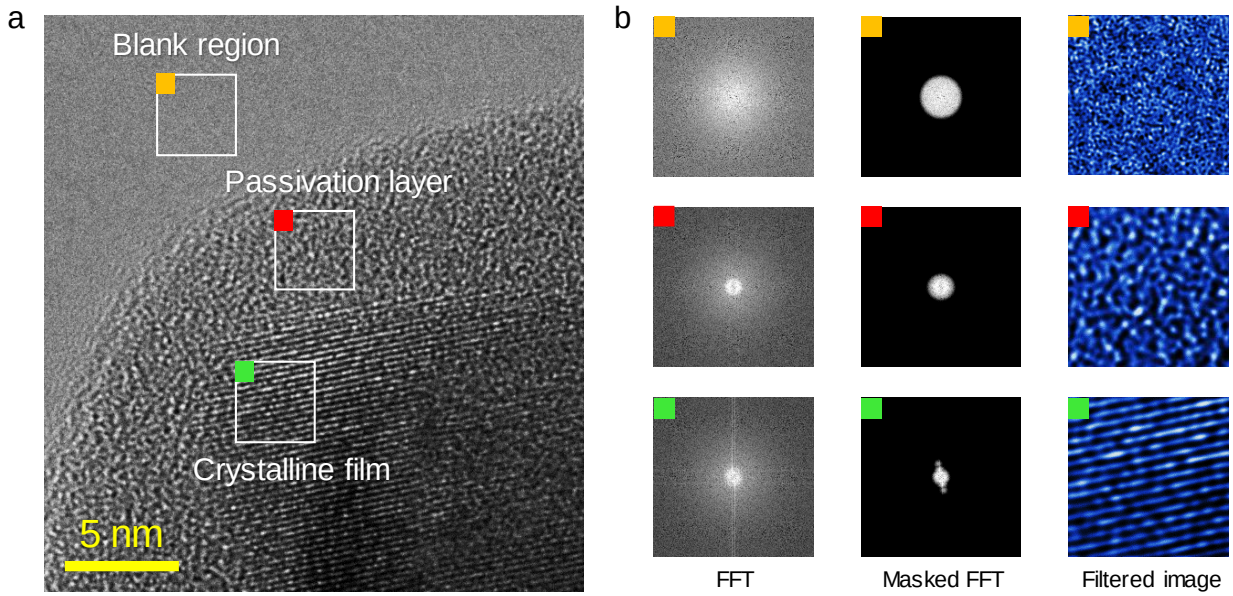

Figure S19. Amorphous passivation layer. (a) HRTEM image of the in-situ grown passivation layer. (b) Filtered HRTEM images from the corresponding regions of (a). Brown, red, and green colors show the blank, amorphous passivation layer, and crystalline bulk regions, respectively.

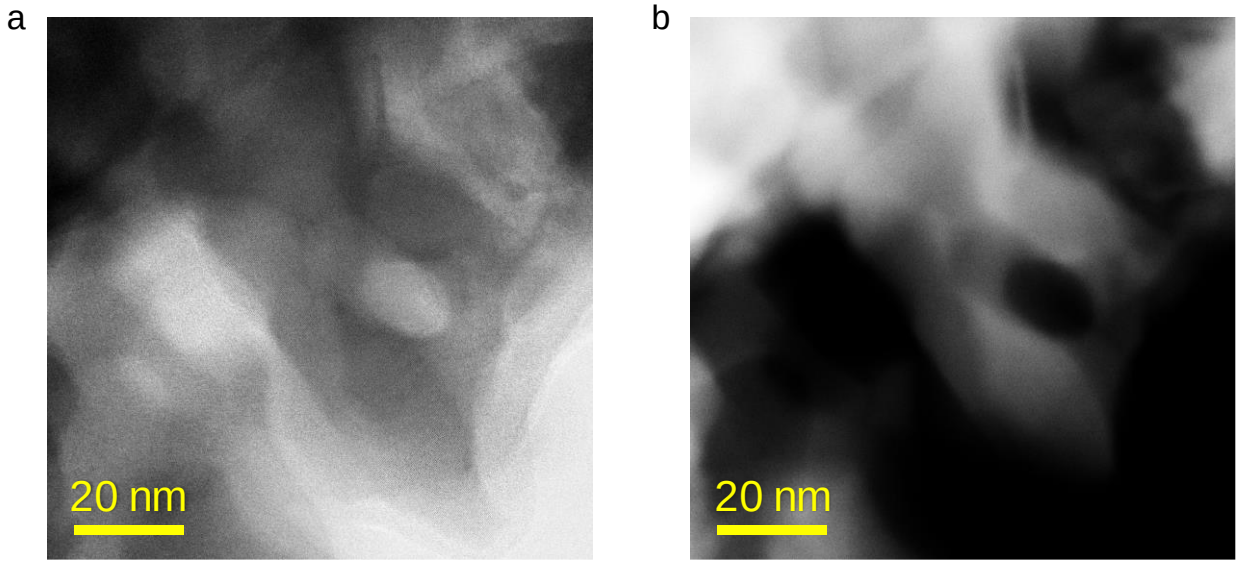

Figure S20. STEM image mode. (a) and (b) Bright- and dark-field STEM images, respectively.

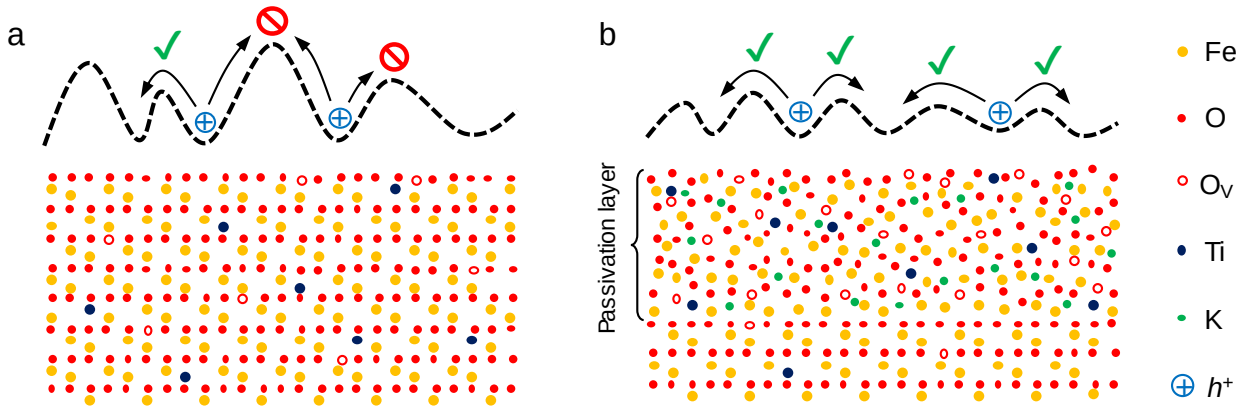

Figure S21. Schematic illustration of the amorphous layer. Schematic illustration of the (a) TFO and (b) EP-TFO electrodes. Top dashed lines in (a) and (b) stand for surface potential fluctuations.

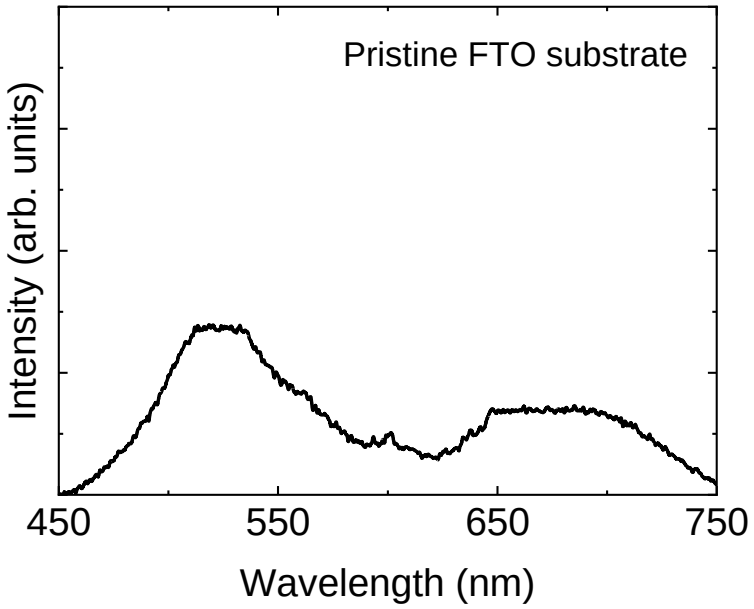

Figure S22. PL spectrum of pristine FTO substrate. PL spectrum of FTO substrate shows two peaks at ~520 nm (intense) and ~675 nm (broad). However, it was suppressed after loading the Ti-doped Fe_2O_3 as shown in Fig. 5b in the main manuscript.

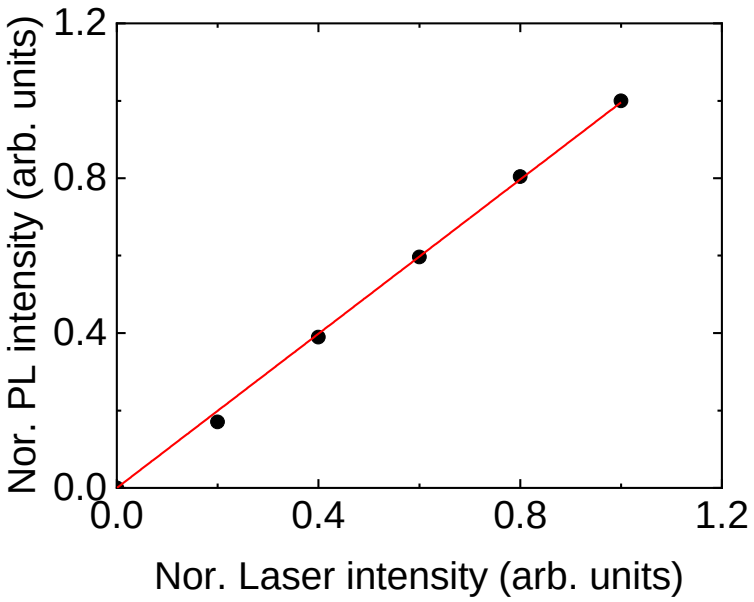

Figure S23. Linear response of the PL signal of the EP-TFO. Total normalized PL intensity versus the normalized laser intensity.

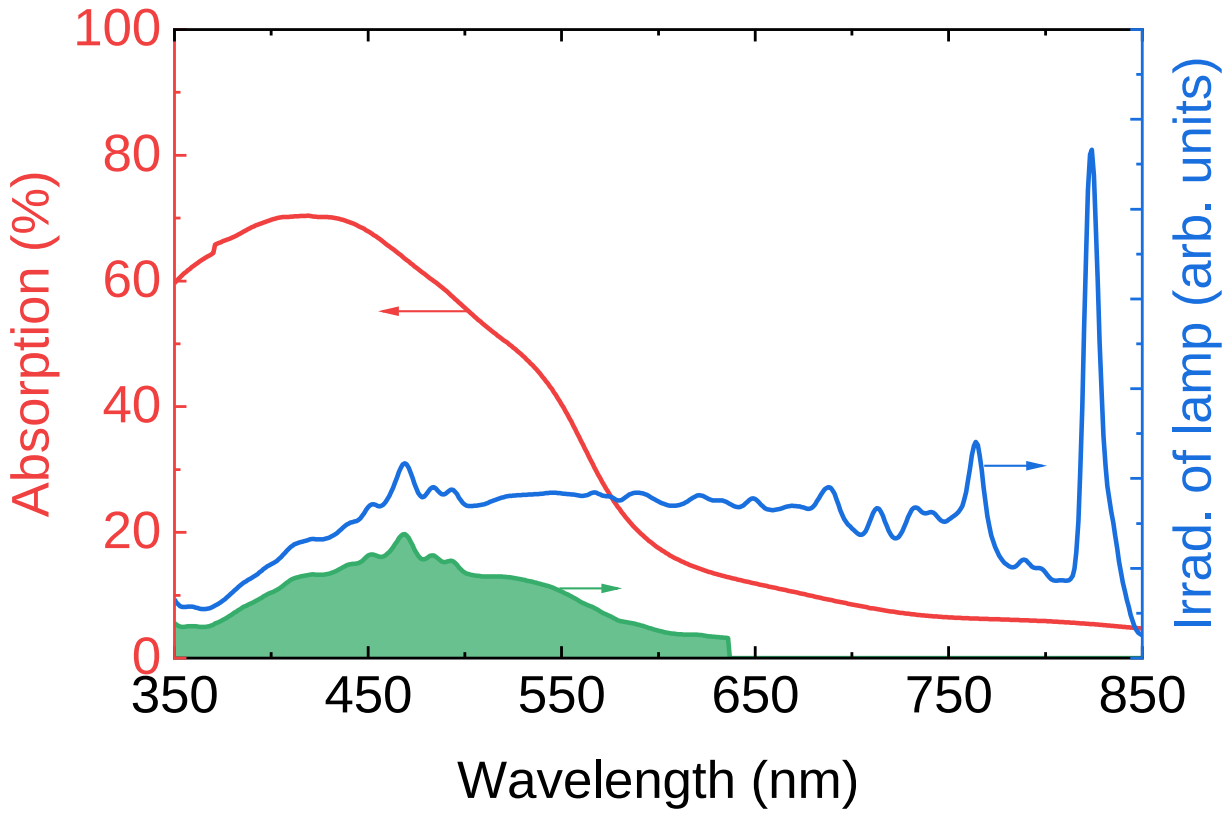

Figure S24. Overall absorption percentage. Absorption (red line), irradiance of the Xe lamp (blue line) spectrum, and absorbable photon flux (green filled curve).

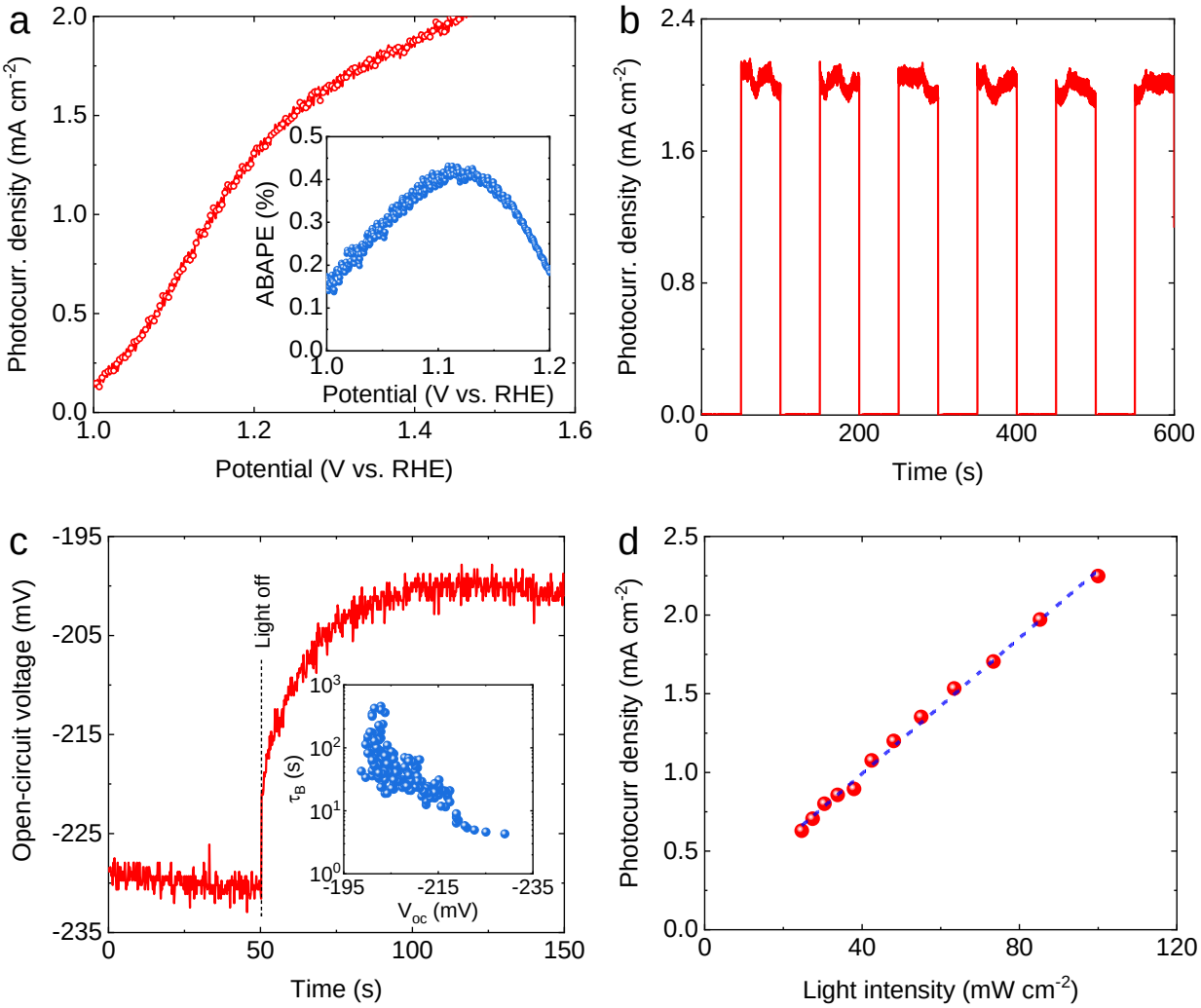

Figure S25. Photoelectrochemical properties of electrochemically passivated TFO photoanode. (a) LSV curve of the photocurrent densities as a function of voltage. The inset shows the ABPE. (b) LSV curve under chopped light irradiation at 1.4 V_{RHE}. (c) OCP in light on–off process. The inset shows potential-dependent carrier lifetimes calculated from the OCP decay in dark. (d) Light intensity-dependent photocurrent density.

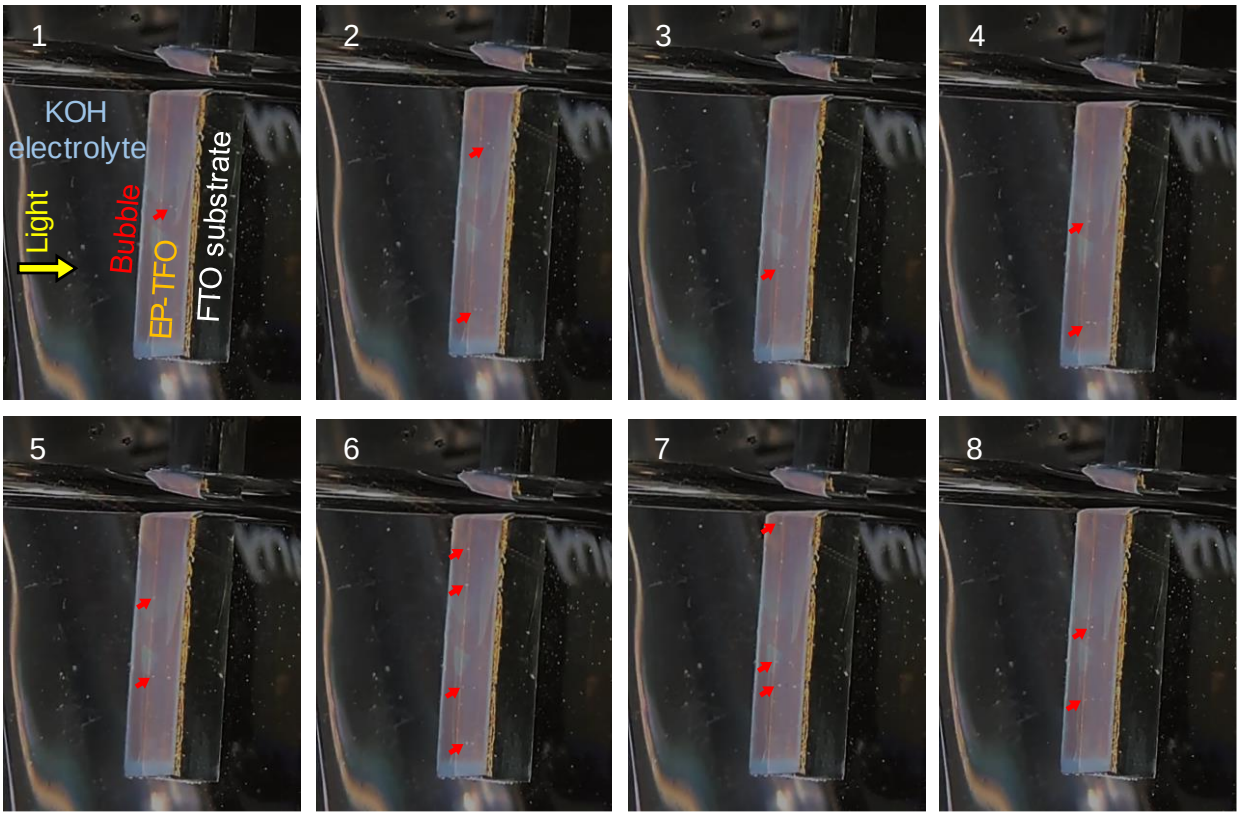

Figure S26. Bubble formation on the surface of photoanode. Snapshots of the PEC process from the surface of the photoanode. Red arrows show the bubble formed on the surface of the EP-TFO.

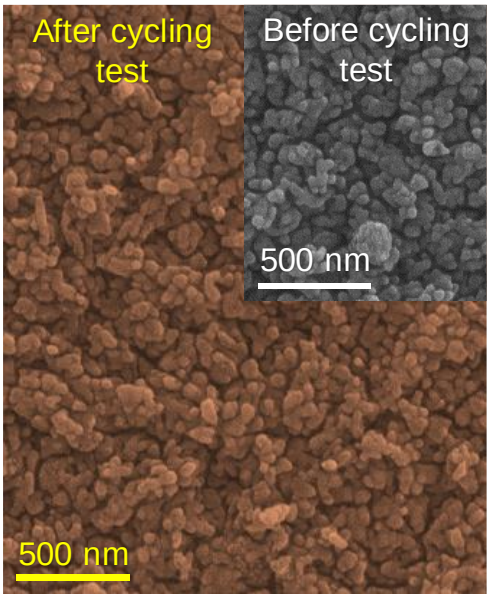

Figure S27. The effect of short-term stability test on the surface morphology. FESEM image of the EP-TFO electrode after cycling test. Inset shows the FESEM image of the photoanode before 10 h stability test.

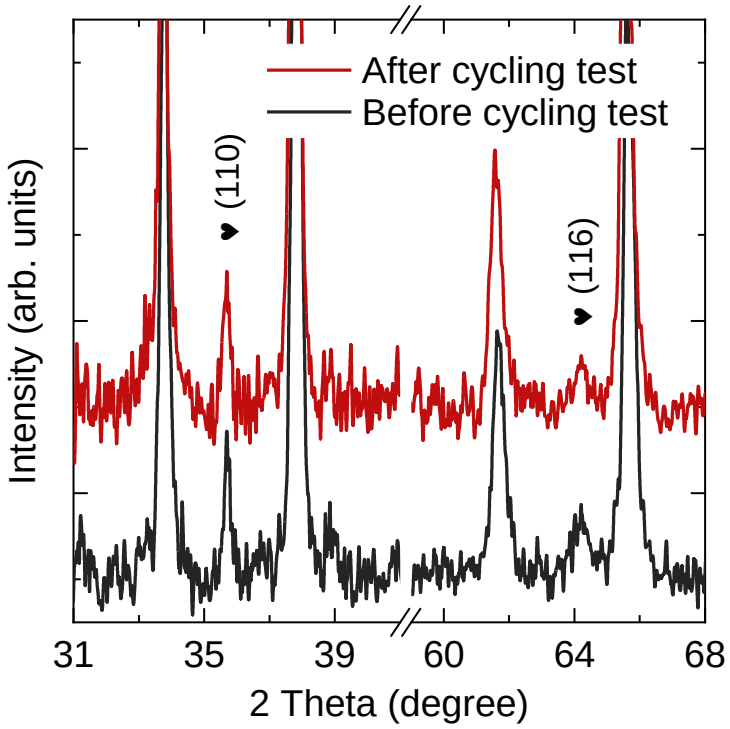

Figure S28. The effect of short-term stability test on the crystal structure. XRD patterns of the EP-FTO before and after 10 h stability test.

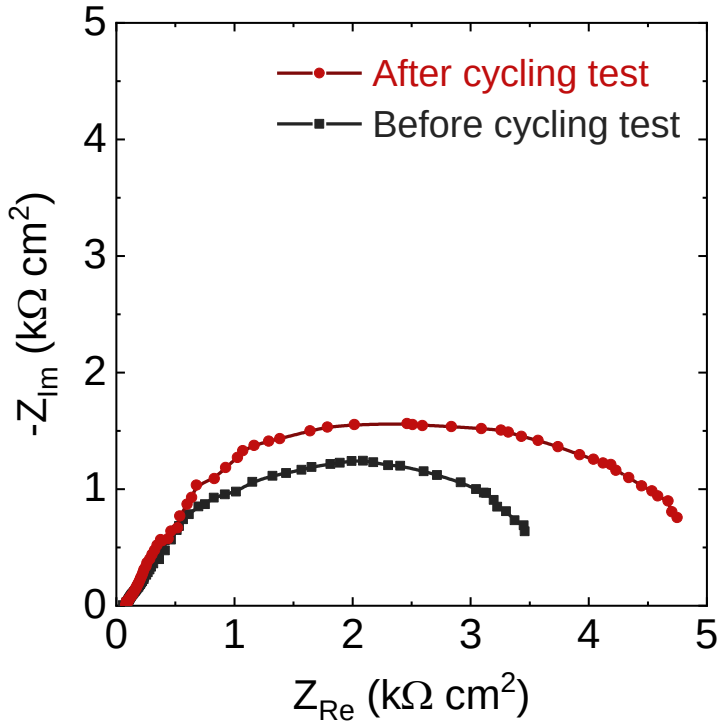

Figure S29. The effect of short-term stability test on the charge transfer. Nyquist plots of the EP-FTO before and after 10 h stability test.

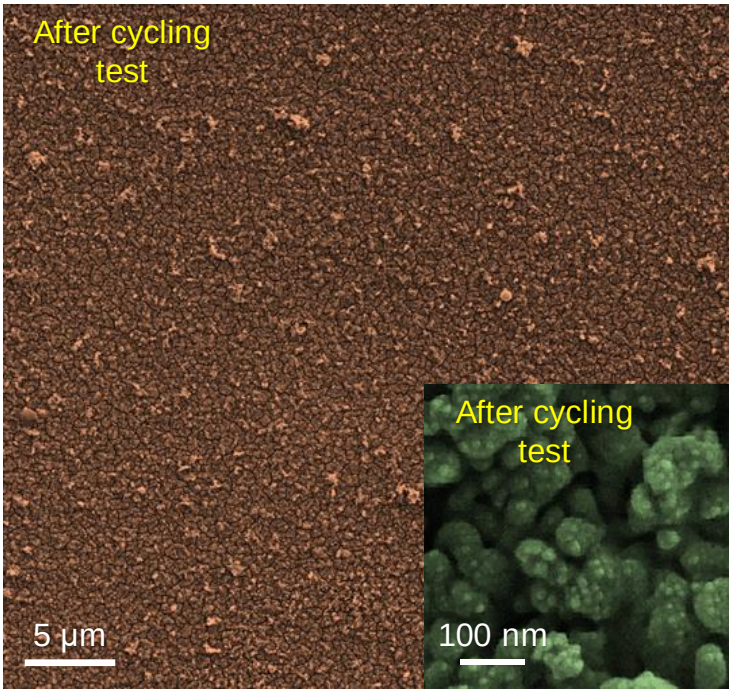

Figure S30. The effect of long-term stability test on the surface morphology. FESEM image of the EP-TFO electrode after 96 h cycling test.

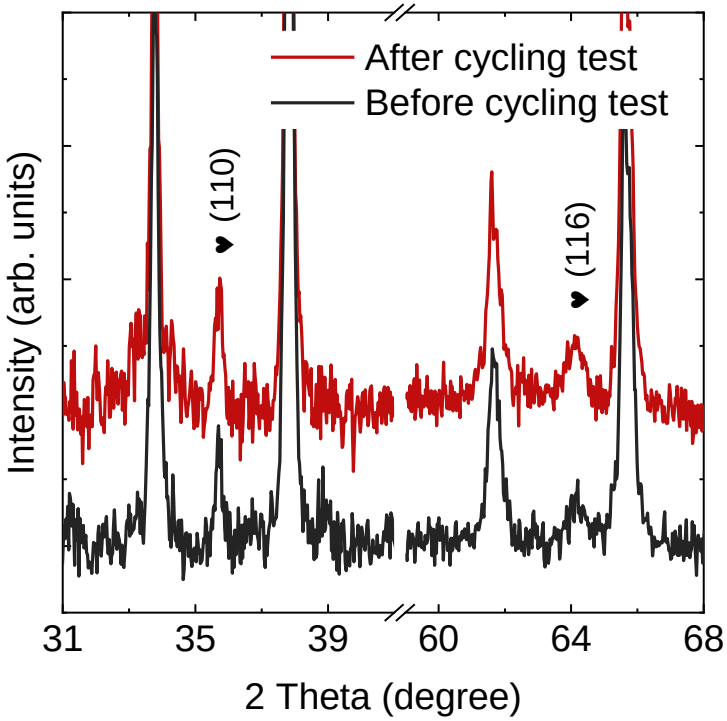

Figure S31. The effect of long-term stability test on the crystal structure. XRD patterns of the EP-FTO before and after 96 h stability test.

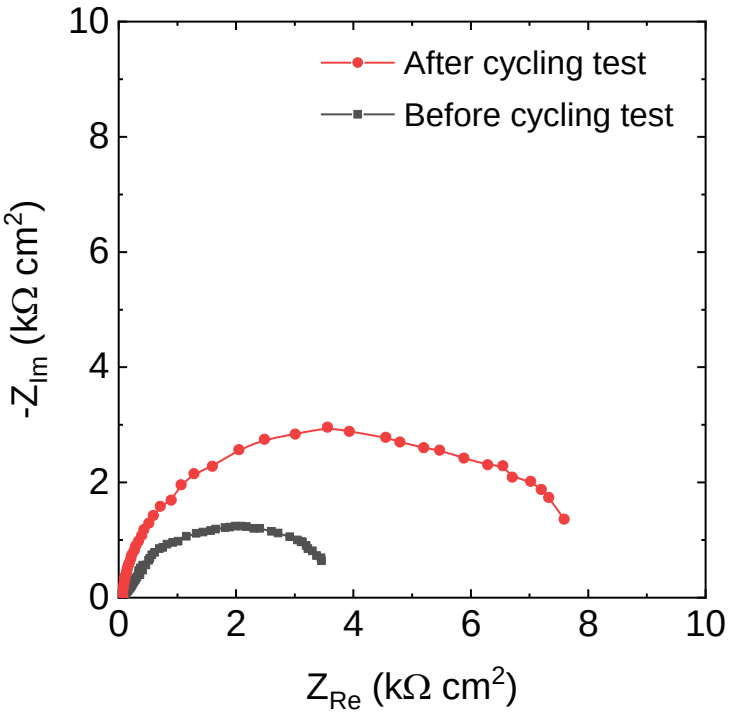

Figure S32. The effect of long-term stability test on the charge transfer. Nyquist plots of the EP-FTO before and after 96 h stability test.

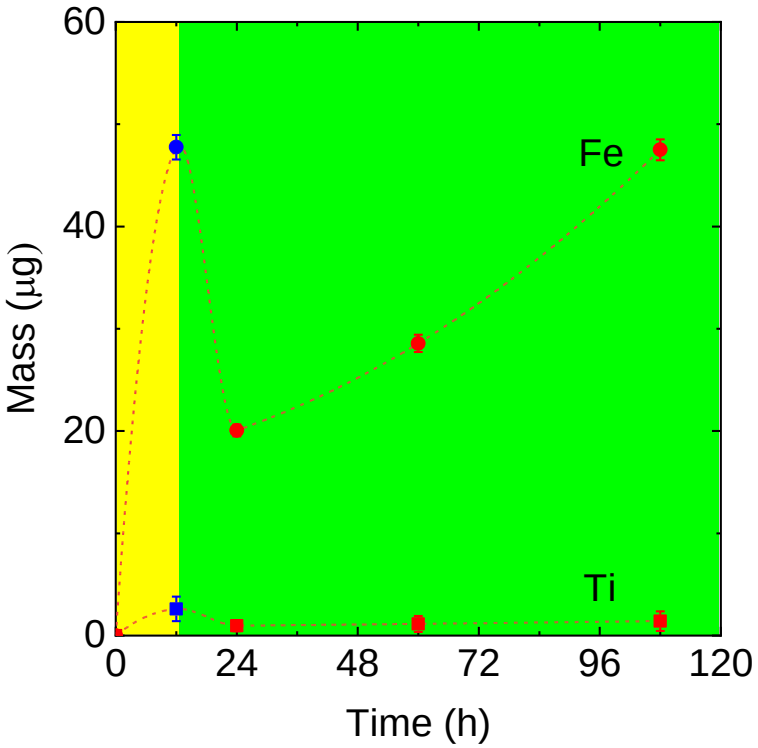

Figure S33. ICP data. Fe and Ti ions release versus time.

Supplementary Tables

Table S1. Examples of photoanodes. Photocurrent response and stability of the hematite-based photoanode materials with the passivation layer and co-catalyst. All the photocurrents are at 1.23 V_{RHE} and under AM 1.5 G light irradiation, i.e. 100 mW cm^{-2}. N/A means not available.

Material & Electrolyte	Passivation layer & Co-catalyst	Synthesis method	Photocurrent ($mA\ cm^{-2}$)	Stability (decay)	Ref.
Ti-Fe_2O_3 1 M KOH	Ti-Fe_2O_{3-x}	In-situ electrochemical process	~1.6 (~2.0 at 1.4 V)	96 h (~5%)	This work
Fe_2O_{3-x} 1 M KOH	MoO_{3-x}	Wet chemical dipping	2.6	4 h (< 20%)	5
Ti-Fe_2O_3 1 M KOH	FeCo-bimetal organic framework	In-situ solvothermal process	2.8	5 h (~ 10%)	10
Ti-Fe_2O_3 1 M KOH	In_2O_3	Wet chemical/annealing	3.4	5 h (< 10%)	11
Fe_2O_3 1 M Na_2SO_4	Al_2O_3/$CuCoO_x$	Chemical water bath	2.23	2 h (< 10%)	4
Ti-Fe_2O_3 N/A	Co-Pi/Fe_2ZrO_5	Hydrothermal	2.88	3 h (< 5%)	12
Ti-Fe_2O_3 1 M KOH	Poly(phenylene oxide)/NiFeOH	Electrodeposition	0.8	15 h (<10%)	13
Sn, Nb-Fe_2O_3 1 M KOH	Nb–O/Sn–O	Electrochemical	3.05	5 h (~7%)	14
CdS/Zr-Fe_2O_3 0.1 M Na_2S + 0.02 M Na_2SO_3	Al_2O_3	Wet chemical dipping	4.2	30 min (< 20%)	15
Ti-Fe_2O_3 1 M NaOH	Al_2O_3	Chemical bath deposition	~2.8	N/A	16
Fe_2O_{3-x} 1 M KOH	TiO_2/Co-Pi	Photodeposition/hydrothermal	6.0	100 h (<10%)	17
Fe_2O_3 1 M NaOH	Co-Pi/Ti-SiO_x	Hydrothermal/annealing	3.19	20 h (< 5%)	18
Fe_2O_3 1 M NaOH	Co-Pi/Ag	Tollens' test method	4.68	2 h (< 10%)	19
Fe_2O_3 1 M NaOH	TiO_2	Atomic layer deposition	~0.65	30 min (< 5%)	20
Fe_2O_3 1 M NaOH	Co^{2+}/Al_2O_3	Atomic layer deposition	~2.0	N/A	21

Table S2. EIS data. Equivalent circuit parameters of the TFO and EP-TFO photoanodes in dark. The reduced chi-square fittings for all samples are ~0.01. R, P, n, and C, which stand for the resistance, constant phase element (CPE), exponent of the CPE, and capacitance, respectively.

Elements	TFO Electrode	EP-TFO Electrode
R_s (Ω cm^2)	21.1	22.2
P (mF Hz^{1-n})	0. 18	0.49
n	0.72	0.56
R_{trap} (kΩ cm^2)	6.90	0.03
C_{ss} (mF cm^{-2})	0. 570	0.166
$R_{ct,ss}$ (kΩ cm^2)	8.41	3.54
C_{sl} (mF cm^{-2})	–	0.009
$R_{ct,sl}$ (kΩ cm^2)	–	1.58

Table S3. Raman data. Peak positions and full width at half maximums (FWHMs) of the fitted peaks of the TFO and EP-TFO samples. Relative peak area (in parentheses) is calculated based on the ratio of the specific peak area to the A_{1g} mode peak area (at ~224 cm^{-1}).

Vibrational mode	TFO Electrode		EP-TFO Electrode	
	ω (cm^{-1})	FWHM (cm^{-1}) (Relative peak area)	ω (cm^{-1})	FWHM (cm^{-1}) (Relative peak area)
A_{1g}	223.4	8.7 (1.00)	224.5	7.3 (1.00)
E_g	243.7	8.6 (0.20)	244.6	7.3 (0.27)
E_g	292.0	17.2 (1.63)	292.8	14.8 (1.58)
E_g	408.2	16.8 (0.90)	409.5	14.7 (0.88)
A_{1g}	497.3	26.3 (0.35)	496.6	19.6 (0.30)
E_g	606.8	23.6 (0.40)	609.2	24.3 (0.50)
E_u^{LO}	658.4	50.9 (0.88)	658.6	46.9 (0.82)

Table S4. XPS data. Peak positions and FWHMs (in parentheses) of Fe 2*p*$_{3/2}$, O 1*s*, and Ti 2*p* of the TFO and EP-TFO samples. All values are in eV unit.

TFO **Fe 2*p*$_{3/2}$**	**EP-TFO** **Fe 2*p*$_{3/2}$**	**TFO** **O 1*s***	**EP-TFO** **O 1*s***	**TFO** **Ti 2*p***	**EP-TFO** **Ti 2*p***	**TFO** **K 2*p***	**EP-TFO** **K 2*p***
708.5 (1.2)	708.0 (1.0)	529.8 (1.0)	529.5 (1.0)	458.1 (1.3)	457.7 (1.3)	–	292.4 (1.3)
709.8 (1.0)	709.6 (1.2)	531.0 (1.2)	530.7 (1.2)	463.8 (2.2)	463.5 (2.2)	–	295.2 (1.2)
710.8 (1.2)	710.7 (1.3)	532.1 (1.3)	531.7 (1.2)				
711.8 (1.4)	711.6 (1.4)	533.1 (1.2)	532.8 (1.2)				
713.0 (1.4)	712.7 (1.5)						
714.4 (2.3)	714.0 (1.6)						
718.9 (4.4)	719.2 (3.0)						

Supplementary References

1 T.-Y. Yang, H.-Y. Kang, K. Jin, S. Park, J.-H. Lee, U. Sim, H.-Y. Jeong, Y.-C. Joo and K. T. Nam, *J. Mater. Chem. A*, 2014, **2**, 2297-2305.

2 H. Y. Du, Y. F. Huang, D. Wong, M. F. Tseng, Y. H. Lee, C. H. Wang, C. L. Lin, G. Hoffmann, K. H. Chen and L. C. Chen, *Nat. Commun.*, 2021, **12**, 1321.

3 D. P. Cao, W. J. Luo, M. X. Li, J. Y. Feng, Z. S. Li and Z. G. Zou, *CrystEngComm*, 2013, **15**, 2386-2391.

4 S. C. Zhang, Z. F. Liu, D. Chen and W. G. Yan, *Appl. Catal. B*, 2020, **277**, 119197.

5 H.-M. Li, Z.-Y. Wang, H.-J. Jing, S.-S. Yi, S.-X. Zhang, X.-Z. Yue, Z.-T. Zhang, H.-X. Lu and D.-L. Chen, *Appl. Catal. B*, 2021, **284**, 119760.

6 X. Zhao, J. Feng, N. Wang, X. Yao, W. Chen, S. Chen, Z. Huang and Z. Chen, *Energy Technol.*, 2018, **6**, 2188-2199.

7 Y. Zeng, Y. Han, Y. Zhao, Y. Zeng, M. Yu, Y. Liu, H. Tang, Y. Tong and X. Lu, *Adv. Energy Mater.*, 2015, **5**, 1402176.

8 A. Kay, I. Cesar and M. Gratzel, *J. Am. Chem. Soc.*, 2006, **128**, 15714-15721.

9 F. Urbach, *Phys. Rev.*, 1953, **92**, 1324-1324.

10 Z. Y. Wang, H. M. Li, S. S. Yi, M. Z. You, H. J. Jing, X. Z. Yue, Z. T. Zhang and D. L. Chen, *Appl. Catal. B*, 2021, **297**, 120406.

11 S.-S. Yi, Z.-Y. Wang, H.-M. Li, Z. Zafar, Z.-T. Zhang, L.-Y. Zhang, D.-L. Chen, Z.-Y. Liu and X.-Z. Yue, *Appl. Catal. B*, 2021, **283**, 119649.

12 T. Jiao, C. Lu, D. Zhang, K. Feng, S. Wang, Z. Kang and J. Zhong, *Appl. Catal. B*, 2020, **269**, 118768.

13 P. Shadabipour and T. W. Hamann, *Chem. Commun.*, 2020, **56**, 2570-2573.

14 H. Zhang, J. H. Park, W. J. Byun, M. H. Song and J. S. Lee, *Chem. Sci.*, 2019, **10**, 10436-10444.

15 M. A. Mahadik, A. Subramanian, H. S. Chung, M. Cho and J. S. Jang, *ChemSusChem*, 2017, **10**, 2030-2039.

16 Z. Fan, Z. Xu, S. Yan and Z. Zou, *J. Mater. Chem. A*, 2017, **5**, 8402-8407.

17 T. H. Jeon, G. H. Moon, H. Park and W. Choi, *Nano Energy*, 2017, **39**, 211-218.

18 H. J. Ahn, K. Y. Yoon, M. J. Kwak and J. H. Jang, *Angew. Chem. Int. Ed. Engl.*, 2016, **55**, 9922-9926.

19 P. Peerakiatkhajohn, J. H. Yun, H. Chen, M. Lyu, T. Butburee and L. Wang, *Adv. Mater.*, 2016, **28**, 6405-6410.

20 X. Yang, R. Liu, C. Du, P. Dai, Z. Zheng and D. Wang, *ACS Appl. Mater. Interfaces*, 2014, **6**, 12005-12011.

21 F. Le Formal, N. Tétreault, M. Cornuz, T. Moehl, M. Grätzel and K. Sivula, *Chem. Sci.*, 2011, **2**, 737-743.